

Structural and Electrical Functionality of NiO Interfacial Films in Bulk Heterojunction Organic Solar Cells

Michael D. Irwin,^{†,‡} Jonathan D. Servaites,^{‡,§} D. Bruce Buchholz,^{‡,§} Benjamin J. Leever,^{‡,||,§} Jun Liu,^{†,§} Jonathan D. Emery,[‡] Ming Zhang,^{‡,§} Jung-Hwan Song,^{§,§} Michael F. Durstock,^{*,||} Arthur J. Freeman,^{*,§,§} Michael J. Bedzyk,^{*,‡,§,⊥} Mark C. Hersam,^{*,†,‡,§} Robert P. H. Chang,^{*,‡,§} Mark A. Ratner,^{*,†,§} and Tobin J. Marks^{*,†,‡,§}

[†]Department of Chemistry, [‡]Department of Materials Science and Engineering and the Materials Research Center, and [§]Department of Physics and Astronomy, Northwestern University, 2145 Sheridan Road, Evanston, Illinois 60208-3113, United States

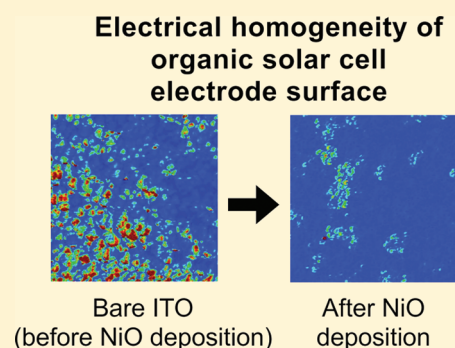
^{||} Air Force Research Laboratory, Wright-Patterson AFB, Ohio 45433, United States

[⊥] Argonne National Laboratory, Argonne, Illinois 60439, United States

[#] Argonne-Northwestern Solar Energy Research Institute, Evanston, Illinois 60208-3113, United States

ABSTRACT: The functionality of NiO interfacial layers in enhancing bulk heterojunction (BHJ) organic photovoltaic (OPV) cell performance is investigated by integrated characterization of the electrical properties, microstructure, electronic structure, and optical properties of thin NiO films grown on glass/ITO electrodes. These NiO layers are found to be advantageous in BHJ OPV applications due to favorable energy band levels, interface passivation, *p*-type character, crystallinity, smooth surfaces, and optical transparency. The NiO overlayers are fabricated via pulsed-laser deposition and found to have a work function of ~ 5.3 eV. They are investigated by both topographic and conductive atomic force microscopy and shown to passivate interfacial charge traps. The films also have an average optical transparency of $>80\%$ in the visible range, crucial for efficient OPV function, and have a near-stoichiometric Ni:O surface composition. By grazing-incidence X-ray diffraction, the NiO thin films are shown to grow preferentially in the (111) direction and to have the fcc NaCl crystal structure. Diodes of *p*-*n* structure and first-principles electronic structure calculations indicate that the NiO interlayer is preferentially conductive to holes, with a lower hole charge carrier effective mass versus that of electrons. Finally, the implications of these attributes in advancing efficiencies for state-of-the-art OPV systems—in particular, improving the open circuit voltage (V_{OC})—are discussed.

KEYWORDS: organic solar cells, nickel oxide, interfacial layer, organic photovoltaics, NiO, hole transport layer, electron blocking layer



I. INTRODUCTION

Organic solar cells (also known as organic photovoltaics, or OPVs) have received increasing attention over the past several years as potential low-cost alternatives to archetypical silicon solar cells.^{1–18} The attraction of OPVs includes compatibility with well-developed, high-throughput thin-film deposition technologies such as roll-to-roll processing,¹⁹ spray coating,²⁰ spin-casting,²¹ and inkjet printing²² for device fabrication. As OPV device efficiency and durability^{23–25} (an often ignored quality) improve progressively with continuous structure optimization and the implementation of new active layer materials, the field is approaching efficient manufacturable technologies.^{26–28} The BHJ cell, as opposed to a bilayer configuration,²⁹ is an intimate blend of donor (D) and acceptor (A) materials that are phase-separated into nanodomains,^{7,12,30,31} where one or both materials absorb photons to form bound electron–hole pairs (excitons). The excitons diffuse to the D–A interfaces where dissociation occurs into free charge carriers, which then travel to their respective electrodes through percolation pathways.^{30,32–37} This architecture

has a significant advantage in that a great proportion of the excitons formed are within the diffusion length (~ 5 – 10 nm)³⁸ of a D–A interface; however, controlling the phase-separated morphology of these systems presents a significant challenge. Optimization of the phase separation process has been achieved empirically via solvent variation,³⁹ annealing,^{31,40,41} controlled drying using high-boiling solvents,²¹ and/or processing additives.⁴²

An inherent limitation of the BHJ nanostructure is that, as a mixed layer, the D and A components can in principle contact both the anode and cathode, potentially permitting the transport of holes and electrons to either electrode and thus creating an environment that risks significant minority carrier collection.^{43–45} Furthermore, ohmic contacts between the active layer and electrodes are typically not established, thereby incurring additional losses. To address these limitations, an interfacial layer (IFL)^{45,46} is frequently applied to the

Received: January 23, 2011

Revised: March 4, 2011

Published: April 01, 2011

| Report Documentation Page | | | | Form Approved OMB No. 0704-0188 | |
|--|------------------------------------|-------------------------------------|---|---|---------------------------------|
| Public reporting burden for the collection of information is estimated to average 1 hour per response, including the time for reviewing instructions, searching existing data sources, gathering and maintaining the data needed, and completing and reviewing the collection of information. Send comments regarding this burden estimate or any other aspect of this collection of information, including suggestions for reducing this burden, to Washington Headquarters Services, Directorate for Information Operations and Reports, 1215 Jefferson Davis Highway, Suite 1204, Arlington VA 22202-4302. Respondents should be aware that notwithstanding any other provision of law, no person shall be subject to a penalty for failing to comply with a collection of information if it does not display a currently valid OMB control number. | | | | | |
| 1. REPORT DATE 01 APR 2011 | | 2. REPORT TYPE | | 3. DATES COVERED 00-00-2011 to 00-00-2011 | |
| 4. TITLE AND SUBTITLE Structural and Electrical Functionality of NiO Interfacial Films in Bulk Heterojunction Organic Solar Cells | | | | 5a. CONTRACT NUMBER | |
| | | | | 5b. GRANT NUMBER | |
| | | | | 5c. PROGRAM ELEMENT NUMBER | |
| 6. AUTHOR(S) | | | | 5d. PROJECT NUMBER | |
| | | | | 5e. TASK NUMBER | |
| | | | | 5f. WORK UNIT NUMBER | |
| 7. PERFORMING ORGANIZATION NAME(S) AND ADDRESS(ES) Northwestern University, Department of Materials Science and Engineering, Evanston, IL, 60208 | | | | 8. PERFORMING ORGANIZATION REPORT NUMBER | |
| 9. SPONSORING/MONITORING AGENCY NAME(S) AND ADDRESS(ES) | | | | 10. SPONSOR/MONITOR'S ACRONYM(S) | |
| | | | | 11. SPONSOR/MONITOR'S REPORT NUMBER(S) | |
| 12. DISTRIBUTION/AVAILABILITY STATEMENT Approved for public release; distribution unlimited | | | | | |
| 13. SUPPLEMENTARY NOTES | | | | | |
| 14. ABSTRACT The functionality of NiO interfacial layers in enhancing bulk heterojunction (BHJ) organic photovoltaic (OPV) cell performance is investigated by integrated characterization of the electrical properties, microstructure, electronic structure, and optical properties of thin NiO films grown on glass/ITO electrodes. These NiO layers are found to be advantageous in BHJ OPV applications due to favorable energy band levels, interface passivation, p-type character, crystallinity smooth surfaces, and optical transparency. The NiO overlayers are fabricated via pulsed-laser deposition and found to have a work function of 5.3 eV. They are investigated by both topographic and conductive atomic force microscopy and shown to passivate interfacial charge traps. The films also have an average optical transparency of >80% in the visible range, crucial for efficient OPV function, and have a near-stoichiometric Ni:O surface composition. By grazing-incidence X-ray diffraction, the NiO thin films are shown to grow preferentially in the (111) direction and to have the fcc NaCl crystal structure. Diodes of p n structure and first-principles electronic structure calculations indicate that the NiO interlayer is preferentially conductive to holes, with a lower hole charge carrier effective mass versus that of electrons. Finally, the implications of these attributes in advancing efficiencies for state-of-the-art OPV systems?in particular, improving the open circuit voltage (VOC)?are discussed. | | | | | |
| 15. SUBJECT TERMS | | | | | |
| 16. SECURITY CLASSIFICATION OF: | | | 17. LIMITATION OF ABSTRACT Same as Report (SAR) | 18. NUMBER OF PAGES 9 | 19a. NAME OF RESPONSIBLE PERSON |
| a. REPORT unclassified | b. ABSTRACT unclassified | c. THIS PAGE unclassified | | | |

anode and again on the active layer prior to cathode deposition. Based on what has been learned from organic light-emitting diode (OLED) research, poly(3,4-ethylenedioxythiophene):poly(styrenesulfonate) (PEDOT:PSS)^{47,48} and LiF⁴⁹ are common materials employed as BHJ OPV IFLs for the anode and cathode, respectively. Although there have been efforts to replace LiF with materials such as TiO_x⁵⁰ and ZnO,^{51,52} replacing PEDOT:PSS is more pressing since it is a known weak link in current BHJ devices. This is a consequence of its electrical and physical inhomogeneity,^{47,48} and interfacial instability arising from its low pH and attendant incompatibility with ITO surfaces (PEDOT:PSS is deposited by spin-coating aqueous suspensions of pH \sim 1).^{23,48,53} Hains et al. established that PEDOT:PSS is a major source of BHJ device failure by thermally stressing identical MDMO-PPV:PCBM active layer OPV devices containing PEDOT:PSS or TPDSi₂:TFB^{54,55} as anode IFLs at 60 °C for 1 h.⁵⁶ The PEDOT:PSS-containing devices fail, while the TPDSi₂:TFB-containing devices exhibit negligible performance degradation. These durability limitations, as well as the opportunity to improve upon PEDOT:PSS device power conversion efficiencies, have provided impetus to replace PEDOT:PSS in OPVs. Therefore, attempts have been made using *n*-type metal oxides,^{45,52,57–59} self-assembled monolayers (SAMs),^{60,61} and the aforementioned *p*-type polymer blends, such as TPDSi₂:TFB^{54–56,62} and PABTSi₂:TFB.⁶³ Anode interfacial layer materials selection should ideally adhere to the following basic guidelines: (1) satisfactory optical transparency in the region of device spectral response, (2) sufficiently high-lying lowest unoccupied molecular orbital (LUMO) or conduction band (CB) to prevent electron leakage to the anode, (3) appropriate highest occupied molecular orbital (HOMO) energy or work function to help facilitate an ohmic contact with the BHJ donor material HOMO, and (4) sufficient hole mobility to function as an effective hole transport layer (HTL).

Nickel oxide, NiO, offers promising attributes as an anode interlayer candidate for OPVs as a wide bandgap, cubic semiconductor, and by virtue of its capacity for electronic tuning by Ni:O stoichiometry control^{64–66} and *p*-type character.^{67–71} Recent reports have demonstrated significant OPV enhancement using NiO anode interlayers.^{44,72–76} However, there is thus far only limited characterization of the microstructure, composition, growth morphology, electronic properties, and the mechanistic function of NiO interlayers that enhance OPV behavior.

In this contribution, we investigate in detail the microstructure, electronic structure, and electrical and optical properties of pulsed-laser deposition-derived NiO interlayers. To achieve this goal, the nanoscopic interlayers are analyzed by atomic force (both topographic and conductive) microscopy, ultraviolet and X-ray photoelectron spectroscopy, grazing-incidence X-ray diffraction, and NiO/Si *p*–*n* junction characteristics. First-principles electronic structure calculations are also carried out on NiO thin slabs. It will be seen from these results that the IFL is composed of near-stoichiometric NiO in a specific fcc(111) growth orientation (for 10 nm thick NiO), it functions effectively as an electron blocking layer (EBL) for photocurrent in BHJ OPV devices, and it homogenizes the anode surface electrically to reduce charge-trap density, while providing good hole transport and optical transparency, excellent film-forming properties, relative chemical inertness, and favorable growth microstructure/electronic structure/carrier transport characteristics.

II. EXPERIMENTAL SECTION

Substrate Preparation. ITO-coated glass (11 Ω/\square) was purchased from Delta Technologies, Ltd., in 25 \times 75 mm strips. Bulk

solvents (ACS grade) for substrate cleaning and HCl (concentrated) for ITO etching were purchased from EMD and used as received. The substrates were patterned to make two electrically separate 3 mm anode strips and 5 mm contact strips by applying a mask and dipping in hot concentrated HCl for 10 s. The substrates were then quenched in saturated NaHCO₃ solution, rinsed, dried, and sonicated in hexanes at 50 °C for 30 min to remove the mask adhesive. The ITO was next cut into 25 \times 12.5 mm substrates and cleaned by sonicating (at 50 °C) in aqueous detergent for 30 min, deionized water for 5 min, methanol, isopropanol, and acetone, sequentially, for 30 min each. The solvent-cleaned substrates were further cleaned, immediately before use as an anode or as a substrate for NiO deposition, in a UV–ozone (UVO) cleaner (Jelight, Inc., Model 42) for 10 min under ambient atmosphere. ITO substrates treated only with solvent cleaning and UVO are the anodes and basis for the samples herein referred to as the “control.”

NiO Film Growth. NiO films were grown by pulsed-laser deposition (PLD), using a 248 nm KrF excimer laser with 25 ns duration and a repetition rate of 2–5 Hz. The 230 mJ/pulse beam was focused onto a 1 mm \times 2 mm spot on the NiO target. The target, \sim 25 mm in diameter, was rotated at 5 rpm and the laser pulses were swept cyclically across the target radius to prevent localized heating. The target–substrate separation was fixed at 10 cm. An O₂ atmosphere at pressures between 2.0×10^{-2} and 2.0×10^{-5} Torr was maintained during the NiO film deposition. The same system was also used for the deposition of gold contacts from a \sim 13 mm diameter metallic gold target: 5 Hz, 135 mJ/pulse, and 5.0×10^{-3} Torr argon deposition ambient. Patterned NiO films were fabricated either by shadow masking or by pre patterning the substrates with AZ-1518 photoresist and postdeposition lift-off. Films patterned by shadow masking were used in the fabrication of solar cells. Films patterned with AZ-1518 were used for step-edge film thickness measurements and fabrication of NiO/*n*-Si diode structures.

Instrumentation. X-ray photoelectron spectroscopy (XPS) data were collected on an Omicron ESCA probe (Omicron, Taunusstein, Germany) equipped with an EA125 energy analyzer. Photoemission was stimulated under ultrahigh vacuum (10^{-8} Torr) with a monochromated Al K α (1486.8 eV) 300 W X-ray source having a circular spot size of \sim 1.5 mm. The incident angle of the photon beam on the sample was fixed at 15° to probe only the atoms nearest the surface. Binding energies of spectra are referenced to the C 1s binding energy set at 284.7 eV. Work functions were measured by Ultraviolet Photoelectron Spectroscopy (UPS) using a Kratos Axis Ultra photoelectron spectrometer with a 21.2 eV He (I) excitation source and a 5 eV pass energy. The UPS spectra were collected while applying a -10 V sample bias to enable the identification of the low kinetic energy edge of the spectrum.

Atomic force microscopy (AFM) data were acquired under ambient conditions with a Veeco Dimension V microscope equipped with an extended tunneling AFM (TUNA) module.⁷⁷ Topographic and conductive AFM images were simultaneously collected in contact mode while applying a $+10$ mV sample bias and using a Budget Sensors ContE Cr/Pt conductive probe. An electrical contact was made to the ITO by contacting a small amount of silver paint applied to the edge of the substrate. Profilometry was performed with a Tencor P-10 profilometer.

Grazing incidence X-ray diffraction (GIXRD) was performed on a Rigaku ATX-G Thin-film Diffraction Workstation at the Northwestern University X-ray Diffraction Facility. The sample was mounted on a 3-axis diffractometer with the sample normal oriented in the horizontal plane. X-rays from a Cu rotating anode vertical line source were conditioned by the parabolic multilayer mirror, which produced a horizontally collimated Cu K α incident beam. To dramatically enhance the scattered signal from the ultrathin film and to extinguish the scattered signal from the substrate, the horizontal incident angle to the sample surface was fixed at $\alpha_i \sim 0.10^\circ$. This is 0.25° below the NiO critical angle ($\alpha_c = 0.35^\circ$). By the evanescent wave effect,^{78,79} this reduces the X-ray penetration depth to ~ 2 nm. The detector arm was

equipped with a soller slit that had a measured vertical divergence of 0.60° . The angular acceptance range for the scattered X-rays in the horizontal direction ranged from 0.0 to 0.9° . This geometry enables acute sensitivity to the ultrathin film and prevents the substrate ITO signal from dominating the diffraction pattern. In this GIXRD geometry, where the 2θ diffractometer axis is along the surface normal of the sample, the incident and scattered wave vectors (\mathbf{k}_0 and \mathbf{k} , respectively) and the resulting scattering vector, $\mathbf{q} = \mathbf{k} - \mathbf{k}_0$, are all essentially constrained to lie in the plane of the film. Diffraction therefore occurs from crystallite planes in the film that are (to within 1°) perpendicular to the surface of the film. The 2θ scan range was from 20° to 90° . Data were background subtracted and normalized to the (200) NiO reflections, and the analysis of integrated peak intensity was performed using a Pseudo-Voigt functional fit.

Current–voltage characterization of NiO/*n*-Si diode structures was performed with a Keithley 237 sourcemeter. Optical spectra were measured with a Varian Instruments Cary 1E spectrophotometer.

NiO Electronic Structure Calculations. Work functions, bandgaps, and charge carrier effective masses of NiO were calculated using the full-potential linearized augmented plane wave (FLAPW) method.^{80,81} The calculations were performed within the local spin density approximation (LSDA),⁸² and the Hedin and Lundqvist form of the exchange correlation potential was used. The LSDA+U method⁸³ (with $U = 8.0$ eV and $J = 0.95$ eV) was also employed to treat the highly correlated Ni 3d electrons and to compare with the LSDA results.

III. RESULTS

The microstructures, morphologies, and electrical/electronic properties of the thin PLD-derived NiO interlayers are analyzed here in detail by grazing incidence X-ray diffraction (GIXRD), topographic and conductive AFM, UPS, and XPS, in *p–n* junction devices, and by FLAPW electronic structure computation. SEM imaging and transmission optical spectroscopy are reported elsewhere.⁴⁴ It will be seen that crystalline fcc NiO at the anode/active layer interface grows with preferential orientation for 5 and 10 nm layer thicknesses.

ITO/NiO XRD. GIXRD was performed to probe film crystal structure and film texturing. Nickel oxide overlayers were grown by PLD on clean glass/ITO substrates. For a layer thickness of 10 nm, the diffraction results reveal a single-phase NiO cubic crystal structure belonging to space group *Fm3m* (NaCl-type) and indicate pronounced preferential fcc(111) crystallite growth with respect to the surface normal (Figure 1). Since GIXRD is sensitive to in-plane crystallite orientation, texturing in the surface normal direction is represented by increases in the integrated intensity from *hkl* reflections that belong to the zone of the textured direction. For example, allowed reflections belonging to the 111 zone are $\bar{2}20$ and $\bar{4}22$. The calculated reflection intensities for a randomly oriented sample predict a ratio of (220):(200) = 0.52, and the experimentally determined ratios for the 10 and 50 nm thick films are 1.1 ± 0.1 and 0.8 ± 0.1 , respectively. This result therefore indicates strong (111) texturing, which decreases with increasing film thickness. Previous $\theta-2\theta$ analyses of 77 nm thick PLD-derived NiO films on glass/ITO revealed random crystalline orientation.⁴⁴ It is also important to note that although the increase in the (220) reflection could indicate (001) texturing, (001) texturing would result in an increase in the (200) signal, which is not observed. The increasing degree of random orientation is also evident for NiO films grown on amorphous substrates. When NiO overlayers are deposited on 1738 float glass, the integrated (220):(200) ratios for 10 and 50 nm thick films are 1.0 ± 0.1 and 0.5 ± 0.1

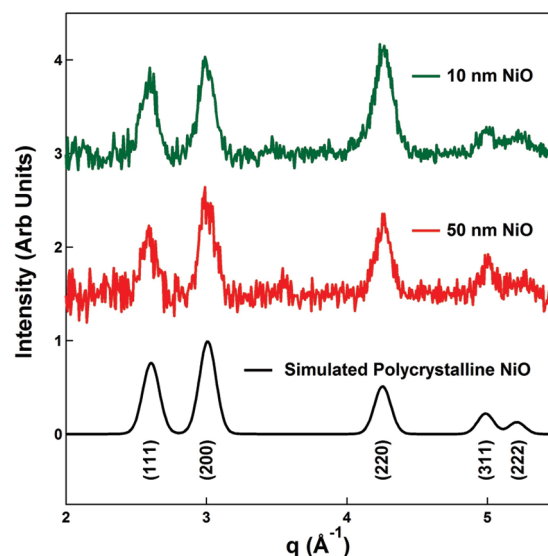


Figure 1. GIXRD patterns calculated for randomly oriented NiO films as well as experimental patterns for 10 and 50 nm thick NiO films grown by PLD on glass/ITO substrates. Cubic NaCl-type NiO (*hkl*) reflections are labeled accordingly. Since GIXRD probes the in-plane structure of the film, increases in the NiO (220) peak intensity represent (111) texturing in the surface-normal direction. Spectra are normalized to the (200) reflection and offset for clarity.

respectively, indicating the ITO substrate imparts significant film texturing.

ITO/NiO AFM/cAFM. The present NiO thin films were cleaned with UVO for 10 min prior to analysis. Immediately observable in the atomic force microscopy is the approximately 50 nm grain size of the 10 nm thick NiO film on ITO (Figure 2c), mirroring the subgrain structure of the underlying ITO film, in contrast to the visible ~ 100 nm grains of the ITO films (Figure 2a). This observation is in agreement with an rms roughness increase from 0.80 nm for the ITO surface to 1.60 nm, after NiO thin-film deposition; this NiO rms roughness is consistent with earlier measurements, while differences in the ITO rms roughnesses reflect batch-to-batch variations from the same supplier.⁴⁴ In the cAFM images of the bare ITO surface, regions of significant differences in conductivity known as “hot spots” and “dead spots” are evident (Figure 2b, at 10 mV, mean current (I_{mean}) = 19.8 nA, $\sigma = 31.1$ nA).^{46,84} This characteristic differs from the NiO images where the variability in conductivity is markedly reduced, along with a significant reduction in I_{mean} at the same applied bias of 10 mV (Figure 2d, $I_{\text{mean}} = 0.343$ pA, $\sigma = 0.336$ pA). Although the conductance of the anode decreases significantly for the NiO/ITO case, the standard deviation of the measured current is low relative to the ITO-only case (i.e., the standard deviation is slightly less than the mean for NiO/ITO, whereas it is more than $1.5\times$ the mean for the ITO-only case). Related work on HCl-treated ITO in OPV devices suggests that improvements of this magnitude in the conductive uniformity of the anode surface likely contribute to enhanced device performance.⁸⁵ While there is some series resistance contribution from the lower surface conductivity in the NiO/ITO case, the reduction in surface traps shown here should counteract the effects of this lower conductance. Additionally, these results highlight the importance of using relatively thin (~ 10 nm) NiO layers to reduce series resistance effects.¹⁶ To verify the accuracy of these measurements, during the course of

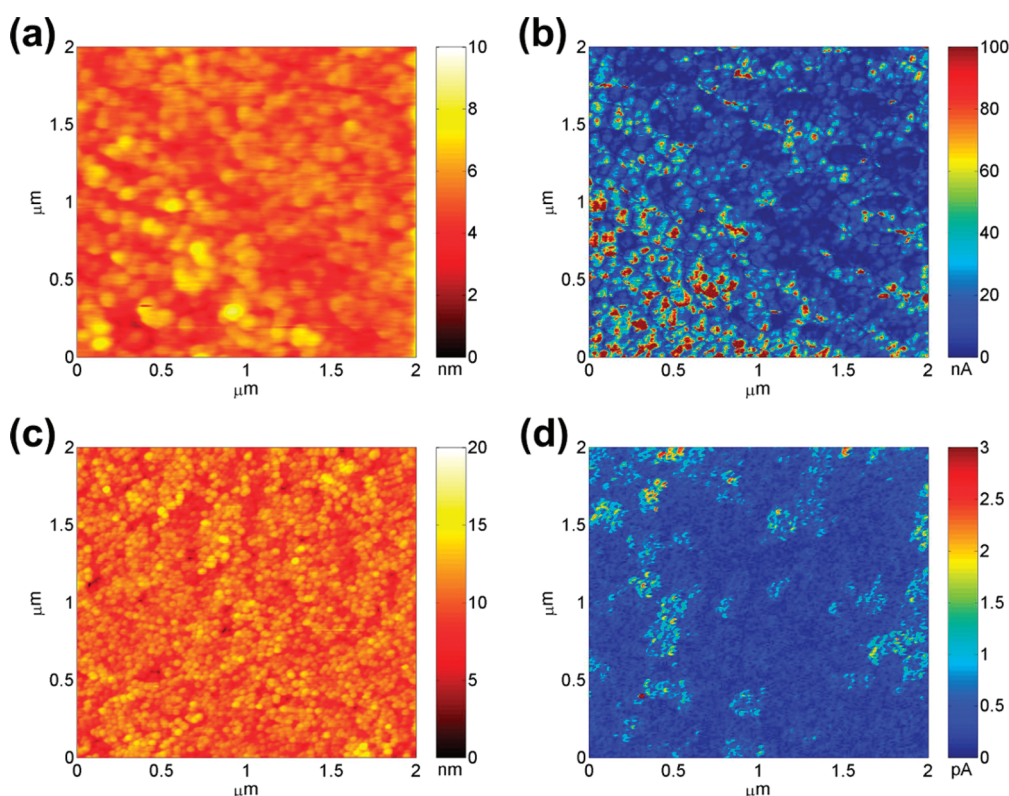


Figure 2. (a) AFM and (b) cAFM images of glass/ITO; (c) AFM and (d) cAFM images of glass/ITO/10 nm NiO (scan areas of $2 \mu\text{m} \times 2 \mu\text{m}$).

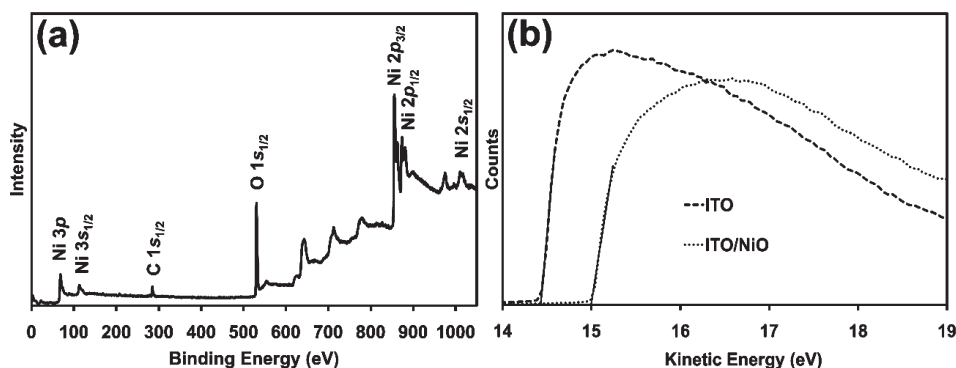


Figure 3. Photoelectron spectra of a 10 nm PLD-derived NiO film grown on glass/ITO. (a) XPS spectrum showing only Ni and O with minor C contamination. The measured Ni:O ratio is 1.1:1.0. (b) UPS spectrum extrapolated to the x-axis revealing a 0.6 eV increase in workfunction compared to ITO. All surfaces were cleaned with 10 min of UVO treatment prior to analysis.

surface characterization, we continuously confirmed that tip integrity was maintained. This was done by testing an ITO sample first, measuring current values of ~ 100 nA. We then measured the NiO and finally returned to the bare ITO sample, repeating the measurements and again observing currents of ~ 100 nA. This process ensures that the significant difference in conductivity between NiO and ITO was correctly observed and that tip integrity was maintained.

ITO/NiO UPS/XPS. The present NiO thin films were cleaned with UVO for 10 min prior to analysis. UPS analysis shows an increase of ~ 0.6 eV in work function when a 10 nm NiO layer is applied to the UVO-treated ITO surface (Figure 3b). When the work function of UVO-treated ITO is referenced to 4.7 eV,^{86,87}

this yields a value of 5.3 ± 0.05 eV for the NiO work function, in agreement with previous reports for NiO films grown by other techniques and on other substrates.^{66,88–92} The composition of the NiO overlayer is found to be near-stoichiometric at $1.1 \pm 0.06:1.0$ Ni:O, with a C:Ni ratio of $0.21 \pm 0.01:1.0$, and free from metallic contaminants by XPS (Figure 3a).

NiO/Si *p–n* Junctions. The in-plane resistance of the present NiO films is greater than the measurement limit of the available van der Pauw apparatus ($6 \text{ M}\Omega/\square$), so a *p–n* diode structure was fabricated, and the *I–V* characteristics were measured to determine whether the NiO films are *p*-type (Figure 4). Contact to the *n*-type Si substrate is found to be near ohmic. The NiO/*n*-Si structure exhibits the *I–V* response typical of a *p–n* diode with

a leakage current, and the NiO/*n*-Si/NiO structure exhibits the *I*–*V* response typical of a *p*–*n*–*p* junction.⁹³

NiO Electronic Structure Calculations. Work Function, Bandgap, and Carrier Effective Mass. For the nonpolar NiO (001) surface calculations, a pristine nine-layer NiO slab was used with a fully optimized two-dimensional geometry. The work function for the nonpolar (001) surface of the nine-layer NiO film is predicted to be approximately 4.71 eV within the LSDA formalism, which is calculated from the valence band (VB) maximum. However, the LSDA+*U*⁹⁴ calculations yield a

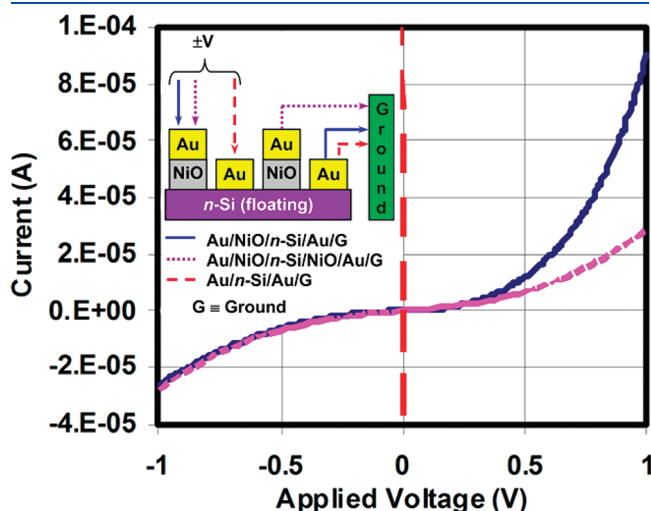


Figure 4. Diode structure used to probe the majority carrier in the PLD-derived NiO thin films. Note the rectifying behavior of the diode structure Au/NiO/*n*-Si/Au.

significantly larger work function value (Figure 5a) of 5.78 eV due to the effects of correlation (i.e., down-shifting of the valence bands). For polar NiO (111) surfaces, it is known that strong surface reconstructions, such as octopolar ($p(2 \times 2)$) surface structures, are operative due to the instability of polar surfaces.⁹⁵ Thus the most stable Ni- and O-terminated octopolar surface structures⁹⁵ were created using symmetric NiO with 11 layers in the (111) orientation, and the geometry was optimized fully. The calculated work functions within the LSDA+*U* formalism (Figure 5a) are 5.44 and 6.83 eV for the Ni and O polar surfaces, respectively.⁹⁶ Compared to the LSDA results, these values are also higher by 0.5 and 1.1 eV for Ni- and O-terminated surfaces, respectively. From the LSDA+*U* results, the polycrystalline NiO films are expected to have a work function of about 6.0 eV.

The bandgaps analyzed with the LSDA+*U* method are computed to be 3.4, 2.9, 1.2, and 1.7 eV for NiO bulk, NiO (001) thin films, Ni-terminated, and O-terminated NiO (111) thin films, respectively, which are significantly greater than the LSDA-derived bandgaps, 0.4 and 0.01 eV for NiO bulk and NiO (001) films, respectively. The polar NiO films analyzed with the LSDA method show metallic surface states. The charge carrier effective masses of bulk NiO were also calculated and can be obtained from the plasma frequency using intraband optical matrix elements.⁹⁶ As shown in Figure 5b, both the LSDA and the LSDA+*U* approaches indicate that the effective masses of the hole carriers are significantly smaller than those of the electron carriers. Especially within the typical ranges of TCO carrier concentrations, $\sim 10^{18}$ – 10^{20} /cm³,^{97,98} the LSDA+*U* calculations show that the effective masses of the carriers are between approximately 0.6 and 1.0, which are consistent with the experimentally measured values.⁹⁹

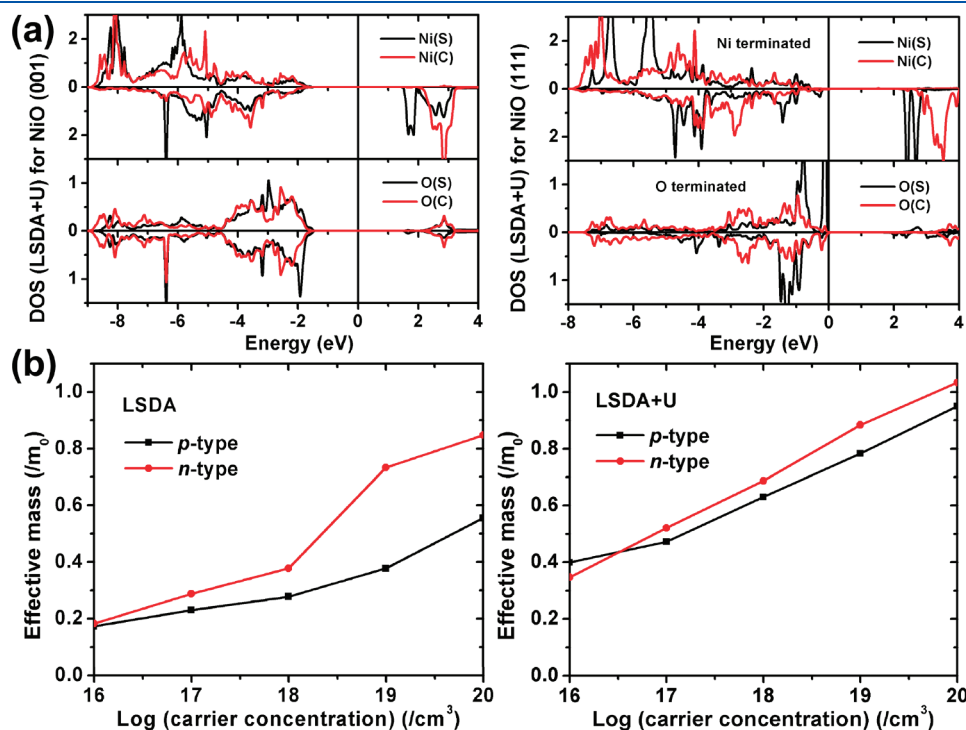


Figure 5. (a) Layer-resolved density of states projected onto Ni d and O p states for NiO (001) and (111) films. S and C indicate the surface and central layers. (b) Effective masses (m/m_0) of NiO for *p*- and *n*-type carriers, where m_0 is the free electron mass.

IV. DISCUSSION

Interfacial “engineering” is a fundamental, generic requirement for efficient operation of all semiconductor devices. For OFETs,^{100–103} OLEDs,^{53–55,64,65,104} and OPVs,^{45,46,49} appropriately designed electrode-active layer interfaces afford faster switching, lower voltage and lower resistance operation, for efficient electron–hole recombination, and enhanced durability. Anode interfacial layer materials selection for optimum OPV function ideally must fulfill the guidelines of (1) good optical transparency in the region of device spectral response, (2) a sufficiently high-lying LUMO or CB to prevent efficiency-eroding electron leakage, (3) an appropriate HOMO energy or work function for near ohmic contact with the HOMO of the organic electron donor material, and (4) a low hole carrier effective mass for efficient hole conduction. Here we present a detailed microstructural and electronic structure analysis showing that PLD-derived NiO interfacial layers on glass/ITO substrates fulfill these requirements necessary for effective interfacial layer behavior in OPVs.

Nickel oxide has a complex, highly correlated electronic structure and is an intrinsic *p*-type semiconductor due to Ni²⁺ vacancies.^{68,99,105,106} By XPS, the NiO surface is found here to be near-stoichiometric with a 1.1:1.0 Ni:O ratio and with an exceptionally low C:Ni ratio of 0.21:1.0, comparable in carbon contamination level to a reactive ion-etched (RIE)/oxygen plasma-cleaned ITO surface. While the measured Ni:O ratio slightly favors Ni, note that the estimated uncertainty in the XPS measurements is ± 0.06 , suggesting that a ratio closer to 1.0:1.0 is possible. Additionally, since XPS is a surface technique, the ratio of the bulk could in principle be somewhat different than the surface. These factors would allow for Ni²⁺ vacancies, which enhance NiO *p*-type conductivity. Previously, the primary experimental evidence that a NiO thin film was present on the ITO surface was from θ – 2θ XRD data for relatively thick 77 nm films grown on ITO.⁴⁴ These early data indicated that the NiO film was randomly oriented and polycrystalline but were of limited relevance since the IFLs in optimized OPVs are far thinner (~ 10 nm). The present GIXRD technique is sensitive to ultrathin film overlayers because the optimized geometry prohibits X-ray penetration into the substrate and thus only detects diffraction from the overlayer. What is found for a 10 nm NiO layer on an ITO substrate is a *structurally ordered NiO film* with preferential growth in the fcc(111) direction (Figure 1). The observation that the NiO layer growth begins with highly crystalline ordering that progressively becomes random in growth direction with increasing film thickness is in accord with the earlier SEM imaging data⁴⁴ where distinct grains appear to merge over the same progression in film thickness.

Optical transparency is an essential characteristic that determines if a material is suitable as an OPV anode interlayer. Previously reported results⁴⁴ indicate that 10 nm of NiO on an ITO/glass substrate maintains a transparency of $\sim 80\%$ for wavelengths ≥ 550 nm, where the active layer oscillator strength is greatest for most OPV systems.^{1,5,26,27} Although the bandgap of the present NiO films is estimated to be 3.6 eV (optical experiment) or 3.4 eV (FLAPW computation), minor absorption is still evident in the visible due to low oscillator strength *d*–*d* transitions.⁴⁴ Note that there is generally a trade-off between transparency and conductivity,¹⁰⁷ and given the essential role of transparency to achieving maximum current densities, it should be important to enhance transparency of the IFL. Series resistance losses due to relatively low conductivity are minimized here by incorporating a relatively thin (~ 10 nm) NiO layer.¹⁶

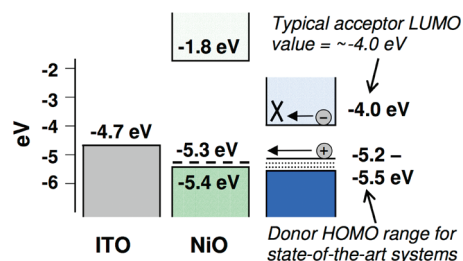


Figure 6. Approximate spatial energy level diagram representing the energy levels, band gaps, and relative position for NiO/ITO relative to the OPV acceptor LUMO level (e.g., PC₇₁BM) and common HOMO levels for state-of-the-art donor systems.^{1,27,42} The NiO energy levels are well-situated to block electron leakage current while promoting hole injection to the ITO.

Another important characteristic for an effective IFL is compatibility with active layer energy levels; that is, the interlayer material should have a sufficiently high-lying CB to provide a barrier to electron collection and yet a sufficiently small work function to effectively collect holes. Referring to Figure 6, with a VB energy of -5.4 eV and a bandgap of 3.6 eV, NiO has a CB energy of -1.8 eV, which in principle should be more than energetically sufficient to block electron leakage from either donor materials or, most importantly, electron-carrying acceptor materials (e.g., PC₇₁BM LUMO = ~ -4.0 eV). To evaluate the work function of the NiO thin films, UPS techniques were employed (Figure 3b), and an increase in NiO work function (Φ) of 0.6 eV is found versus a clean ITO surface. Referencing to $\Phi_{\text{ITO}} = 4.7$ eV,^{61,86} $\Phi_{\text{NiO}} = 5.3$ eV is then determined. This result is comparable to values reported in the literature for NiO films grown by other techniques and on other substrates^{66,88–92} and is reasonably within the range of several state-of-the-art donor systems (Figure 6).^{1,27,42} By reducing photocurrent recombination at the anode, it is expected that an effective EBL will enhance V_{OC} ; these V_{OC} enhancements relative to control samples have been demonstrated by several research groups, including this one, in recent NiO OPV reports.^{44,72,73}

Note that based on the approximate device energy level diagram in Figure 6, there is not always perfect alignment between the relevant NiO levels and the donor HOMO level (common range of -5.2 to -5.5 eV shown in Figure 6). However, it is also important to note that these energies may be somewhat different in the actual BHJ blend versus values measured for the individual materials; there are three plausible reasons for this. First, the donor HOMO energy levels are typically estimated from cyclic voltammetry,²⁶ for which molecular solvation effects cannot be explicitly compensated, as opposed to UPS data which are acquired under high vacuum on a pristine surface on the bulk materials, avoiding solvation effects and accounting for intermolecular bulk interactions. Second, there is the potential for a vacuum level shift induced by interfacial dipoles at the NiO/organic interface.¹¹² If this effect were substantial, the desired energy level alignment could be achieved. Lastly, Fermi level pinning arising from donor surface states could also compensate for the observed energetic differences.^{108–110}

The final requirement for an anode IFL is that the material exhibit efficient hole transport and *p*-type behavior. In the present study, diodes were fabricated having the structure Au/NiO/*n*-Si/Au (Figure 4) and were found to be preferentially conductive to forward bias, versus diodes of the structure

Au/NiO/*n*-Si/NiO/Au that are equally resistive to forward and reverse bias.⁷⁰ This rectifying behavior indicates that NiO thin films grown under the present conditions are in fact *p*-type. Furthermore, additional support for this conclusion is provided by electronic structure modeling. Applying both the LSDA and LSDA+U formalisms (Figure 5b), the electron effective mass (m/m_0) is found to be greater than the hole effective mass over the carrier concentration range 10^{17} – 10^{20} /cm³, consistent with *p*-type character and EBL/HTL function.^{111,112} These observations are also consistent with the report by Zunger et al.⁶⁸ showing that NiO is *p*-dopable but not *n*-dopable. NiO differs markedly in this electronic structure characteristic from high-valent early transition metal oxide IFL materials such as V₂O₅ and MoO₃.^{57,113} MoO₃ has recently been shown to have far lower-lying conduction and valence bands than NiO and to be strongly *n*-type. It would be expected to be far more efficient at hole injection into/electron extraction from relatively electron-rich organic π -systems than the inverse.¹¹³

The primary objective of EBL introduction is to increase V_{OC} and, hence, OPV power conversion efficiency. The origin of V_{OC} in OPVs has long been debated; however, it is now generally accepted that, in the case of ohmic contacts, it originates primarily from the difference in energy between the donor HOMO and the acceptor LUMO, the principle diode.^{43,114} However, it has been observed that V_{OC} values are typically ~ 300 – 400 mV less than this HOMO–LUMO energy level difference.¹¹⁴ This loss can be ascribed to the presence of recombination sources in addition to the donor–acceptor interface, as well as the density of states profile of the donor and acceptor materials.¹¹² These recombination sources can include surface states and injection barriers at the electrode interfaces or impurities in the active layer. As seen in the cAFM images, NiO has a significant electrical homogenization effect on the ITO anode surface (Figure 2b,d) with a pronounced reduction of the ITO “hot spots”—spikes in conductivity—and “dead spots”—troughs of resistivity.⁸⁴ This variation in conductivity is thought to be a source of surface states destructive to charge carriers, and thus a homogenized surface should increase V_{OC} . As also noted above, the high-lying CB of NiO should suppress the collection of minority carrier electrons at the anode. Thus, NiO interlayers have demonstrated significant V_{OC} increases in previous OPV reports, when compared to bare ITO.

V. CONCLUSIONS

Through a multifaceted combination of microstructural, electrical, and computational electronic structure analysis, the microstructure, function, and opto-electronic roles of thin PLD-derived NiO films as an EBL/HTL in BHJ OPVs are clarified. It is shown here that NiO grows as smooth, crystalline, oriented thin films on ITO substrates to form an optically near-transparent anode coating. These thin films also electrically homogenize the ITO anode surface, forming an electrically homogenizing, passivating, semiconducting interlayer, which prevents anode electron injection and promotes anode hole injection. Photoelectron spectroscopy (XPS/UPS) reveals a near-stoichiometric surface with a work function of 5.3 eV and very low carbon contamination. FLAPW calculations based on the LSDA and LSDA+U formalisms reveal a low hole carrier effective mass versus the electron carrier effective mass and confirm the experimentally derived work function and bandgap. Ultimately, these attributes lead to enhanced OPV efficiencies, primarily via increased device open circuit voltages.

AUTHOR INFORMATION

Corresponding Author

*E-mail: t-marks@northwestern.edu (T.J.M.); Michael.Durstock@wpafb.af.mil (M.F.D.); ajf328@northwestern.edu (A.J.F.); bedzyk@northwestern.edu (M.J.B.); m-hersam@northwestern.edu (M.C.H.); r-chang@northwestern.edu (R.P.H.C.); ratner@northwestern.edu (M.A.R.).

ACKNOWLEDGMENT

We thank BP Solar, the AFRL Materials & Manufacturing Directorate, the DOE (DE-FG02-06ER46320), the Army Research Office (W911NF-05-1-0177), the NSF (ECS-0609064), and the ANSER Energy Frontier Research Center (funded by the Department of Energy, DE-SC0001059) for support of this research. We thank the NSF-MRSEC program through the Northwestern Materials Research Center (DMR-0520513) for support of characterization facilities.

REFERENCES

- (1) Chen, H. Y.; Hou, J. H.; Zhang, S. Q.; Liang, Y. Y.; Yang, G. W.; Yang, Y.; Yu, L. P.; Wu, Y.; Li, G. *Nat. Photonics* **2009**, *3*, 649.
- (2) He, Y. J.; Chen, H. Y.; Hou, J. H.; Li, Y. F. *J. Am. Chem. Soc.* **2010**, *132*, 5532.
- (3) Helgesen, M.; Sondergaard, R.; Krebs, F. C. *J. Mater. Chem.* **2010**, *20*, 36.
- (4) Heremans, P.; Cheyns, D.; Rand, B. P. *Acc. Chem. Res.* **2009**, *42*, 1740.
- (5) Hou, J.; Chen, H.-Y.; Zhang, S.; Chen, R. I.; Yang, Y.; Wu, Y.; Li, G. *J. Am. Chem. Soc.* **2009**, *131*, 15586.
- (6) Zou, Y. P.; Najari, A.; Berrouard, P.; Beaupre, S.; Aich, B. R.; Tao, Y.; Leclerc, M. *J. Am. Chem. Soc.* **2010**, *132*, 5330.
- (7) Brabec, C. J.; Durrant, J. R. *MRS Bull.* **2008**, *33*, 670.
- (8) Cai, W. Z.; Gong, X.; Cao, Y. *Sol. Energy Mater. Sol. Cells* **2010**, *94*, 114.
- (9) Dennler, G.; Lungenschmied, C.; Neugebauer, H.; Sariciftci, N. S.; Labouret, A. *J. Mater. Res.* **2005**, *20*, 3224.
- (10) Gaudiana, R.; Brabec, C. *Nat. Photonics* **2008**, *2*, 287.
- (11) Gledhill, S. E.; Scott, B.; Gregg, B. A. *J. Mater. Res.* **2005**, *20*, 3167.
- (12) Guenes, S.; Neugebauer, H.; Sariciftci, N. S. *Chem. Rev.* **2007**, *107*, 1324.
- (13) Kroon, R.; Lenes, M.; Hummelen, J. C.; Blom, P. W. M.; de Boer, B. *Polym. Rev.* **2008**, *48*, 531.
- (14) Shaheen, S. E.; Ginley, D. S.; Jabbour, G. E. *MRS Bull.* **2005**, *30*, 10.
- (15) Thompson, B. C.; Frechet, J. M. J. *Angew. Chem., Int. Ed.* **2008**, *47*, 58.
- (16) Servaites, J. D.; Yeganeh, S.; Marks, T. J.; Ratner, M. A. *Adv. Funct. Mater.* **2010**, *20*, 97.
- (17) Morton, O. *Nature* **2006**, *443*, 19.
- (18) Jen, A. K. Y. *J. Mater. Chem.* **2010**, *20*, 2491.
- (19) Tobjork, D.; Aarnio, H.; Makela, T.; Osterbacka, R. *Mater. Res. Soc. Symp. Proc.* **2008**, *1091E*, 1091.
- (20) Green, R.; Morfa, A.; Ferguson, A. J.; Kopidakis, N.; Rumbles, G.; Shaheen, S. E. *Appl. Phys. Lett.* **2008**, *92*, 033301.
- (21) Li, G.; Shrotriya, V.; Huang, J.; Yao, Y.; Moriarty, T.; Emery, K.; Yang, Y. *Nat. Mater.* **2005**, *4*, 864.
- (22) Steirer, K. X.; Berry, J. J.; Reese, M. O.; van Hest, M. F. A. M.; Miedaner, A.; Liberatore, M. W.; Collins, R. T.; Ginley, D. S. *Thin Solid Films* **2009**, *517*, 2781.
- (23) Girtan, M.; Rusu, M. *Sol. Energy Mater. Sol. Cells* **2010**, *94*, 446.
- (24) Jorgensen, M.; Norrman, K.; Krebs, F. C. *Sol. Energy Mater. Sol. Cells* **2008**, *92*, 686.

- (25) Vitoratos, E.; Sakkopoulos, S.; Dalas, E.; Paliatsas, N.; Kara-georgopoulos, D.; Petraki, F.; Kennou, S.; Choulis, S. A. *Org. Electron.* **2009**, *10*, 61.
- (26) Dennler, G.; Scharber, M. C.; Brabec, C. J. *Adv. Mater.* **2009**, *21*, 1323.
- (27) Liang, Y. Y.; Xu, Z.; Xia, J. B.; Tsai, S. T.; Wu, Y.; Li, G.; Ray, C.; Yu, L. P. *Adv. Mater.* **2010**, *22*, E135.
- (28) Servaites, J. D.; Ratner, M. A.; Marks, T. J. *Appl. Phys. Lett.* **2009**, *95*, 163302.
- (29) Tang, C. W. *Appl. Phys. Lett.* **1986**, *48*, 183.
- (30) Ma, W.; Gopinathan, A.; Heeger, A. J. *Adv. Mater.* **2007**, *19*, 3656.
- (31) Yang, X.; Loos, J.; Veenstra, S. C.; Verhees, W. J. H.; Wienk, M. M.; Kroon, J. M.; Michels, M. A. J.; Janssen, R. A. J. *Nano Lett.* **2005**, *5*, 579.
- (32) Dante, M.; Peet, J.; Nguyen, T.-Q. *J. Phys. Chem. C* **2008**, *112*, 7241.
- (33) Mihailetchi, V. D.; Xie, H.; de Boer, B.; Popescu, L. M.; Hummelen, J. C.; Blom, P. W. M.; Koster, L. J. A. *Appl. Phys. Lett.* **2006**, *89*, 012107.
- (34) Morana, M.; Wegscheider, M.; Bonanni, A.; Kopidakis, N.; Shaheen, S.; Scharber, M.; Zhu, Z.; Waller, D.; Gaudiana, R.; Brabec, C. *Adv. Funct. Mater.* **2008**, *18*, 1757.
- (35) Pivrikas, A.; Sariciftci, N. S.; Juska, G.; Osterbacka, R. *Prog. Photovoltaics* **2007**, *15*, 677.
- (36) Xin, H.; Ren, G.; Kim, F. S.; Jenekhe, S. A. *Chem. Mater.* **2008**, *20*, 6199.
- (37) Coakley, K. M.; McGehee, M. D. *Chem. Mater.* **2004**, *16*, 4533.
- (38) Halls, J. J. M.; Pichler, K.; Friend, R. H.; Moratti, S. C.; Holmes, A. B. *Appl. Phys. Lett.* **1996**, *68*, 3120.
- (39) Rispens, M. T.; Meetsma, A.; Rittberger, R.; Brabec, C. J.; Sariciftci, N. S.; Hummelen, J. C. *Chem. Commun.* **2003**, 2116.
- (40) Ma, W.; Yang, C.; Gong, X.; Lee, K.; Heeger, A. J. *Adv. Funct. Mater.* **2005**, *15*, 1617.
- (41) Li, G.; Shrotriya, V.; Yao, Y.; Yang, Y. *J. Appl. Phys.* **2005**, *98*, 043704.
- (42) Lee, J. K.; Ma, W. L.; Brabec, C. J.; Yuen, J.; Moon, J. S.; Kim, J. Y.; Lee, K.; Bazan, G. C.; Heeger, A. J. *J. Am. Chem. Soc.* **2008**, *130*, 3619.
- (43) Moliton, A.; Nunzi, J.-M. *Polym. Int.* **2006**, *55*, 583.
- (44) Irwin, M. D.; Buchholz, D. B.; Hains, A. W.; Chang, R. P. H.; Marks, T. J. *Proc. Natl. Acad. Sci. U.S.A.* **2008**, *105*, 2783.
- (45) Chen, L. M.; Xu, Z.; Hong, Z. R.; Yang, Y. *J. Mater. Chem.* **2010**, *20*, 2575.
- (46) Steim, R.; Kogler, F. R.; Brabec, C. J. *J. Mater. Chem.* **2010**, *20*, 2499.
- (47) Kemerink, M.; Timpanaro, S.; De Kok, M. M.; Meulenkaamp, E. A.; Touwslager, F. J. *J. Phys. Chem. B* **2004**, *108*, 18820.
- (48) Kim, Y.-H.; Lee, S.-H.; Noh, J.; Han, S.-H. *Thin Solid Films* **2006**, *510*, 305.
- (49) Ahlswede, E.; Hanisch, J.; Powalla, M. *Appl. Phys. Lett.* **2007**, *90*, 163504.
- (50) Kim, J. Y.; Kim, S. H.; Lee, H.-H.; Lee, K.; Ma, W.; Gong, X.; Heeger, A. J. *Adv. Mater.* **2006**, *18*, 572.
- (51) Gilot, J.; Barbu, I.; Wienk, M. M.; Janssen, R. A. J. *Appl. Phys. Lett.* **2007**, *91*, 113520.
- (52) White, M. S.; Olson, D. C.; Shaheen, S. E.; Kopidakis, N.; Ginley, D. S. *Appl. Phys. Lett.* **2006**, *89*, 143517.
- (53) Ni, J.; Yan, H.; Wang, A.; Yang, Y.; Stern, C. L.; Metz, A. W.; Jin, S.; Wang, L.; Marks, T. J.; Ireland, J. R.; Kannewurf, C. R. *J. Am. Chem. Soc.* **2005**, *127*, 5613.
- (54) Huang, Q.; Evmenenko, G. A.; Dutta, P.; Lee, P.; Armstrong, N. R.; Marks, T. J. *J. Am. Chem. Soc.* **2005**, *127*, 10227.
- (55) Yan, H.; Lee, P.; Armstrong, N. R.; Graham, A.; Evmenenko, G. A.; Dutta, P.; Marks, T. J. *J. Am. Chem. Soc.* **2005**, *127*, 3172.
- (56) Hains, A. W.; Liu, J.; Martinson, A. B. F.; Irwin, M. D.; Marks, T. J. *Adv. Funct. Mater.* **2010**, *20*, 595.
- (57) Shrotriya, V.; Li, G.; Yao, Y.; Chu, C.-W.; Yang, Y. *Appl. Phys. Lett.* **2006**, *88*, 073508.
- (58) Hancox, I.; Chauhan, K. V.; Sullivan, P.; Hatton, R. A.; Moshar, A.; Mulcahy, C. P. A.; Jones, T. S. *Energy Environ. Sci.* **2010**, *3*, 107.
- (59) Kim, D. Y.; Subbiah, J.; Sarasqueta, G.; So, F.; Ding, H. J.; Irfan; Gao, Y. L. *Appl. Phys. Lett.* **2009**, *95*, 093304.
- (60) Hau, S. K.; Yip, H.-L.; Ma, H.; Jen, A. K. Y. *Appl. Phys. Lett.* **2008**, *93*, 233304.
- (61) Kim, J. S.; Park, J. H.; Lee, J. H.; Jo, J.; Kim, D.-Y.; Cho, K. *Appl. Phys. Lett.* **2007**, *91*, 112111.
- (62) Hains, A. W.; Marks, T. J. *Appl. Phys. Lett.* **2008**, *92*, 023504.
- (63) Hains, A. W.; Ramanan, C.; Irwin, M. D.; Liu, J.; Wasielewski, M. R.; Marks, T. J. *ACS Appl. Mater. Interfaces* **2010**, *2*, 175.
- (64) Chan, I. M.; Hsu, T.-Y.; Hong, F. C. *Appl. Phys. Lett.* **2002**, *81*, 1899.
- (65) Im, H. C.; Choo, D. C.; Kim, T. W.; Kim, J. H.; Seo, J. H.; Kim, Y. K. *Thin Solid Films* **2007**, *515*, S099.
- (66) Nakasa, A.; Adachi, M.; Usami, H.; Suzuki, E.; Taniguchi, Y. *Thin Solid Films* **2006**, *498*, 240.
- (67) Hardee, K. L.; Bard, A. J. *J. Electrochem. Soc.* **1977**, *124*, 215.
- (68) Lany, S.; Osorio-Guillen, J.; Zunger, A. *Phys. Rev. B* **2007**, *75*, 241203/1.
- (69) Nakaoka, K.; Ueyama, J.; Ogura, K. *J. Electroanal. Chem.* **2004**, *571*, 93.
- (70) Ohta, H.; Kamiya, M.; Kamiya, T.; Hirano, M.; Hosono, H. *Thin Solid Films* **2003**, *445*, 317.
- (71) Chan, I. M.; Hsu, T. Y.; Hong, F. C. *Appl. Phys. Lett.* **2002**, *81*, 1899.
- (72) Wang, Z. Y.; Lee, S. H.; Kim, D. H.; Kim, J. H.; Park, J. G. *Sol. Energy Mater. Sol. Cells* **2010**, *94*, 1591.
- (73) Steirer, K. X.; Chesin, J. P.; Widjonarko, N. E.; Berry, J. J.; Miedaner, A.; Ginley, D. S.; Olson, D. C. *Org. Electron.* **2010**, *11*, 1414.
- (74) Betancur, R.; Maymó, M.; Elias, X.; Vuong, L. T.; Martorell, J. *Sol. Energy Mater. Sol. Cells* **2011**, *95*, 735.
- (75) Sun, N.; Fang, G.; Qin, P.; Zheng, Q.; Wang, M.; Fan, X.; Cheng, F.; Wan, J.; Zhao, X. *Sol. Energy Mater. Sol. Cells* **2010**, *94*, 2328.
- (76) Sun, N. H.; Fang, G. J.; Qin, P. L.; Zheng, Q. A.; Wang, M. J.; Fan, X.; Cheng, F.; Wan, J. W.; Zhao, X. Z.; Liu, J. W.; Carroll, D. L.; Ye, J. M. *J. Phys. D: Appl. Phys.* **2010**, *43*.
- (77) Leever, B. J.; Durstock, M. F.; Irwin, M. D.; Hains, A. W.; Marks, T. J.; Pingree, L. S. C.; Hersam, M. C. *Appl. Phys. Lett.* **2008**, *92*, 013302.
- (78) Becker, R. S.; Golovchenko, J. A.; Patel, J. R. *Phys. Rev. Lett.* **1983**, *50*, 153.
- (79) Dosch, H.; Batterman, B. W.; Wack, D. C. *Phys. Rev. Lett.* **1986**, *56*, 1144.
- (80) Jansen, H. J. F.; Freeman, A. J. *Phys. Rev. B* **1984**, *30*, 561.
- (81) Wimmer, E.; Krakauer, H.; Weinert, M.; Freeman, A. J. *Phys. Rev. B* **1981**, *24*, 864.
- (82) Hedin, L.; Lundqvist, B. I. *J. Phys. C: Solid State Phys.* **1971**, *4*, 2064.
- (83) Shick, A. B.; Liechtenstein, A. I.; Pickett, W. E. *Phys. Rev. B* **1999**, *60*, 10763.
- (84) Steim, R.; Choulis, S. A.; Schilinsky, P.; Lemmer, U.; Brabec, C. J. *Appl. Phys. Lett.* **2009**, *94*, 043304.
- (85) Irwin, M. D.; Liu, J.; Leever, B. J.; Servaites, J. D.; Hersam, M. C.; Durstock, M. F.; Marks, T. J. *Langmuir* **2010**, *26*, 2584.
- (86) Kim, J. S.; Lagel, B.; Moons, E.; Johansson, N.; Baikie, I. D.; Salaneck, W. R.; Friend, R. H.; Cacialli, F. *Synth. Met.* **2000**, *111–112*, 311.
- (87) Milliron, D. J.; Hill, I. G.; Shen, C.; Kahn, A.; Schwartz, J. J. *Appl. Phys.* **2000**, *87*, 572.
- (88) Olivier, J.; Servet, B.; Vergnolle, M.; Mosca, M.; Garry, G. *Synth. Met.* **2001**, *122*, 87.
- (89) Wei, B.; Yamamoto, S.; Ichikawa, M.; Li, C.; Fukuda, T.; Taniguchi, Y. *Semicond. Sci. Technol.* **2007**, *22*, 788.
- (90) Huefner, S. *Adv. Phys.* **1994**, *43*, 183.

- (91) Huefner, S.; Steiner, P.; Sander, I.; Reinert, F.; Schmitt, H.; Neumann, M.; Witzel, S. *Solid State Commun.* **1991**, *80*, 869.
- (92) Patil, P. S.; Kadam, L. D. *Appl. Surf. Sci.* **2002**, *199*, 211.
- (93) Baca, A. G. *Character. Mater.* **2003**, *1*, 466.
- (94) Benegone, O.; Alouani, M.; Blochl, P.; Hungel, J. *Los Alamos Natl. Lab., Prepr. Arch., Condens. Matter* **2000**, 1.
- (95) Zhang, W.-B.; Tang, B.-Y. *J. Chem. Phys.* **2008**, *128*, 124703.
- (96) Ambrosch-Draxl, C.; Sofo, J. O. *Comput. Phys. Commun.* **2006**, *175*, 1.
- (97) Gordon, R. G. *MRS Bull.* **2000**, *25*, 52.
- (98) Minami, T. *Thin Solid Films* **2008**, *516*, 1314.
- (99) Choi, S. C.; Koumoto, K.; Yanagida, H. *J. Mater. Sci.* **1986**, *21*, 1947.
- (100) DiBenedetto, S. A.; Frattarelli, D.; Ratner, M. A.; Facchetti, A.; Marks, T. J. *J. Am. Chem. Soc.* **2008**, *130*, 7528.
- (101) Hayakawa, R.; Petit, M.; Chikyow, T.; Wakayama, Y. *Appl. Phys. Lett.* **2008**, *93*, 153301.
- (102) Singh, T. B.; Koeppe, R.; Sariciftci, N. S.; Morana, M.; Brabec, C. J. *Adv. Funct. Mater.* **2009**, *19*, 789.
- (103) Zhang, X.-H.; Kippelen, B. *J. Appl. Phys.* **2008**, *104*, 104504.
- (104) Huang, Q.; Evmenenko, G.; Dutta, P.; Marks, T. J. *J. Am. Chem. Soc.* **2003**, *125*, 14704.
- (105) McKay, J. M.; Henrich, V. E. *Phys. Rev. B* **1985**, *32*, 6764.
- (106) Pizzini, S.; Morlotti, R. *J. Electrochem. Soc.* **1967**, *114*, 1179.
- (107) Tate, J.; Jayaraj, M. K.; Draeseke, A. D.; Ulbrich, T.; Sleight, A. W.; Vanaja, K. A.; Nagarajan, R.; Wager, J. F.; Hoffman, R. L. *Thin Solid Films* **2002**, *411*, 119.
- (108) Bisquert, J.; Garcia-Belmonte, G.; Munar, A.; Sessolo, M.; Soriano, A.; Bolink, H. J. *Chem. Phys. Lett.* **2008**, *465*, 57.
- (109) Hao, X. T.; Hosokai, T.; Mitsuo, N.; Kera, S.; Mase, K.; Okudaira, K. K.; Ueno, N. *Appl. Phys. Lett.* **2006**, *89*, 182113.
- (110) Xu, Z.; Chen, L.-M.; Chen, M.-H.; Li, G.; Yang, Y. *Appl. Phys. Lett.* **2009**, *95*, 013301.
- (111) Offermans, T.; Meskers, S. C. J.; Janssen, R. A. J. *Proc. SPIE* **2005**, 5938, 593812.
- (112) Blom, P. W. M.; Mihailetchi, V. D.; Koster, L. J. A.; Markov, D. E. *Adv. Mater.* **2007**, *19*, 1551.
- (113) Kroger, M.; Hamwi, S.; Meyer, J.; Riedl, T.; Kowalsky, W.; Kahn, A. *Appl. Phys. Lett.* **2009**, *95*, 123301.
- (114) Scharber, M. C.; Wuhlbacher, D.; Koppe, M.; Denk, P.; Waldauf, C.; Heeger, A. J.; Brabec, C. L. *Adv. Mater.* **2006**, *18*, 789.